



Performance of small-scale bladeless electromagnetic energy harvesters driven by water or air



Dan Zhao*, Chenzhen Ji, C. Teo, Shihuai Li

Division of Aerospace Engineering, College of Engineering, Nanyang Technological University, Singapore 639798, Singapore

ARTICLE INFO

Article history:

Received 8 September 2013

Received in revised form

20 March 2014

Accepted 2 April 2014

Available online 26 April 2014

Keywords:

Electromagnetic

Bladeless harvester

Energy harvesting

Hydropower

Rainwater

ABSTRACT

In this work, three different-diameter energy harvesters driven by turbulent air flow and rainwater are designed. Experiments are conducted first on the air-driven harvesters to gain insight on the energy conversion process. Unlike conventional blade-involved systems, the present setup involves using a number of co-rotating compact discs. They are closely spaced and attached to a central shaft, on which a magnet is attached. As the air flow excitations are set to 4 different levels, the harvester performances are measured in both open- and closed-loop electrical circuits. The results show that approximately 0.3 W electricity is produced. Parametric analysis is then conducted to highlight the effect of the system parameters, such as disc diameter, number, exhaust flow rates and inter-disc distance on its performance and to gain insight on its optimum design. Numerical simulations are then conducted to understand the flow physics. Finally, a 40 mm harvester is used to harness energy from rainwater. Compared with the same size air-driven harvester, the rainwater-driven one is working more efficiently in terms of the overall energy conversion efficiency. The maximum electric current is about 4.5 mA. A practical demonstration is then conducted by using the electricity generated to power a red light-emitting diode (LED).

© 2014 Elsevier Ltd. All rights reserved.

1. Introduction

Currently, there is a need for the development of energy harvesters so that ambient energy can be converted into electricity to meet the increased energy demand arising from the development and wide application of electronic devices. Various energy harvesting techniques have been developed to achieve this task. Typically, these techniques take advantage of thermoacoustic [1–9], magnetoelectric [10], piezoelectric [11,12], thermoelectric [13,14] or optoelectric working principles. One of the interesting ideas is to harness the mechanical energy of rainwater or air flow [15,16].

The technology to harvest wind energy or hydropower [15,16] is well-developed by using wind or water turbines. Some of the turbines such as impulse water turbines convert the kinetic energy by rotating large-diameter blades (with unit in meter). Wind energy and hydropower utilization systems as reliable energy sources have become major power generation industries in the last two decades. The energy generated from those systems has increased

dramatically. Since the performance of wind/water turbines depends strongly on the hydrodynamic characteristics of runner blades [15], the optimum design of the blade profiles and angle of attack need to be determined. The performance of different blade profiles at different wind speeds and angles of attack was investigated by using finite volume computational method [17] to solve Reynolds-averaged Navier–Stokes equations.

Wind farm and hydropower advocate favor developments in the context global warming abatement. However the direct or indirect effects on wildlife (aquatic life), or the local concerns of visual intrusion are not addressed. In addition, aero- or hydrodynamic noise is of a real annoying issue for large wind or water harvester. The effects on the wild/aquatic life, and the 'sensed visual or noise impact' may contribute to the social opposition to large wind/water harvesters. Thus 'small' or 'micro' harvesters [18,19] are becoming more and more popular due to the high power to weight ratio and reduced visual and ecological impacts in comparison with the large harvesting systems.

Conventional air- or water-driven energy harvesters involve using large-diameter blades (>1 m) [20]. However, bladeless energy harvesters [21–28] might be as efficient and reliable as those bladed ones. The working fluid is injected nearly tangentially to the bladeless systems with rotating discs. The injected fluid passes

* Corresponding author. N3-02c-72, Division of Aerospace Engineering, 50 Nanyang Avenue, Singapore 639798, Singapore.

E-mail address: zhaodan@ntu.edu.sg (D. Zhao).

through the narrow gaps between the discs and approaches spirally towards the exhaust orifices located at the center of each disc [27]. The viscous drag force generated due to the relative velocity between the disc and the flowing fluid, causes the disc to rotate. The rotating discs are enclosed in a casing with a small radial and axial clearance. The bladeless system has many advantages [28,29]: easy and cheap to manufacture and maintain, low cost, and significantly reduced noise impact on environments. It can produce power from a variety of working media, like water or air, or mixed fluids. All these features indicate that the bladeless system can be used for the development of a miniature energy harvesting system.

Like many other tropical countries, Singapore receives abundant rainfall throughout the year. The average annual rainfall of Singapore is about 2400 mm. Such rainfall is a source of 'green' energy, which has great potential to be harnessed, especially for rainwater collection systems applied in Singapore. In this work, small-scale energy harvesters driven by air or water are designed. Experimental tests of air-driven harvesters are first conducted to gain insights on its working principles. Three different diameter harvesters are studied, as the inlet volume flow rate is set to 4 different values. This is described in Sect. 2.1. The working principles and numerical simulations are discussed in Sect. 2.2. The harnessed electrical power can be measured in open- or closed-loop electrical circuit configuration, as discussed in Sect. 2.3. In addition, four design parameters are identified. In Sect. 3, experimental results are shown and discussed. Finally, in Sect. 4, the potential of applying such miniature bladeless system for harvesting energy from rainwater is experimentally investigated. Comparison is then made between the rainwater-driven harvester and the same-size air-driven one.

2. Description of experiments

2.1. Experimental setup

A bladeless electromagnetic energy harvester driven by turbulent air flow is designed and experimentally tested first, with the overall aim of exploring an alternative system for harvesting the mechanical energy of rainwater flow. The energy harvesting system (see Fig. 1(a)) involves using a number of co-rotating CDs (compact discs), as shown in Fig. 1(b). They are evenly spaced in the axial direction and attached to a central shaft, on which a magnet is attached. The inter-disc distance can be varied from 0.2 mm to 3.5 mm. In addition, three harvesters with different disc diameters are built: 120 mm, 80 mm and 40 mm. The smallest disc is chosen

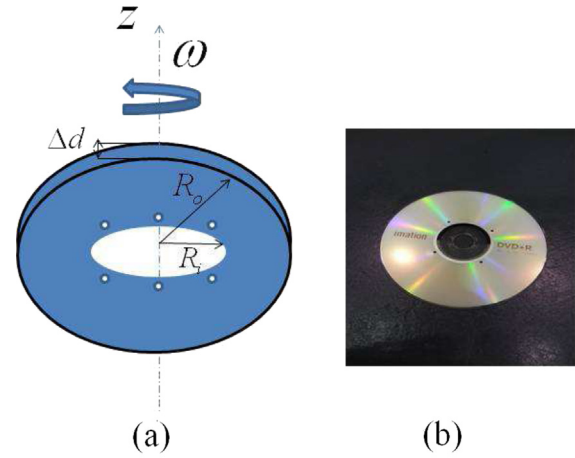


Fig. 2. (a) Schematic diagram of two neighboring discs, (b) photo of a 120 mm disc with exhaust orifices.

to be 40 mm so that the disc diameters of the three harvesters are changed with a constant step size of 40 mm.

2.2. Working principles and numerical simulations

The bladeless system works due to the fact that a viscous drag force is generated due to the velocity gradient present between a compact disc and working fluid acting in the direction of the relative velocity of the fluid. Assuming the fluid is injected at a velocity \mathbf{U} through a stationary disc as shown in Fig. 2(a), the relative velocity of the disc is $-\mathbf{U}$. The viscous drag force on the discs will act in the direction of the fluid flow, opposing the motion of the fluid. Since there is a relative velocity between the working fluid and the disc wall, a velocity gradient near the wall is present. It is responsible for the generation of shear stress τ_w :

$$\tau_w(r) = \mu_f \frac{\partial \mathbf{U}_\theta(r, z)}{\partial z} \quad (1)$$

The shear stress τ_w gives rise to a torque Π on the disc, which can be calculated by integrating the elemental torque as

$$\Pi = 2 \int_0^{2\pi} d\theta \int_{R_i}^{R_o} \tau_w(r) r^2 dr \quad (2)$$

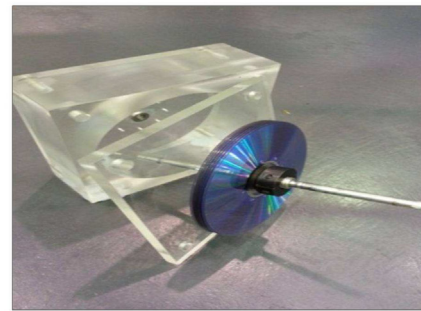
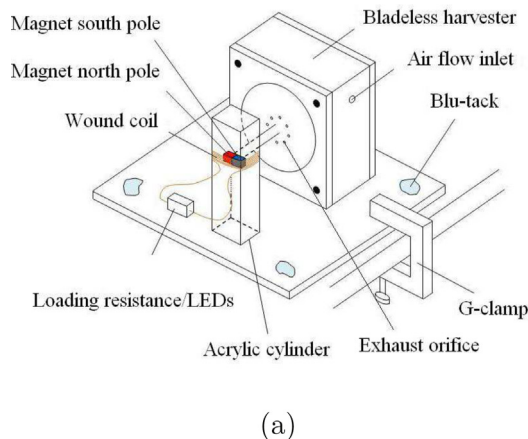


Fig. 1. (a) Schematic of a bladeless electromagnetic energy harvester, (b) photo of compact discs.

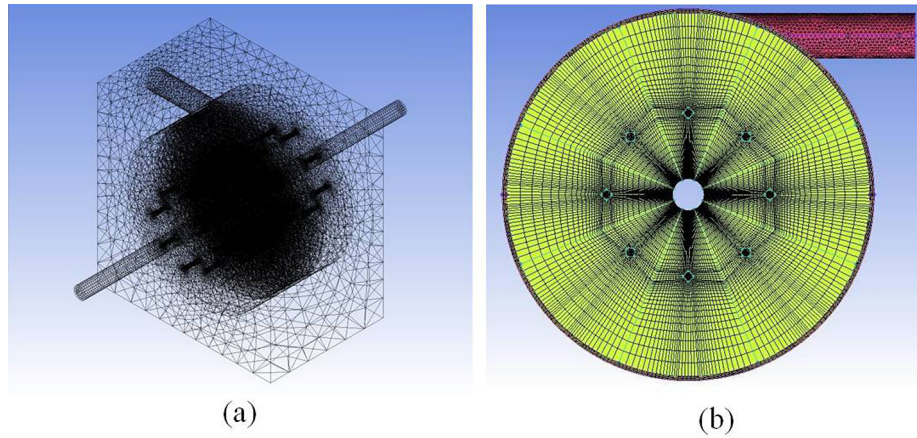


Fig. 3. Mesh generated for CFD simulations.

If the torque Π is greater than the frictional torque, the discs start rotating. As the disc speed increases, the relative velocity of the fluid with respect to the disc decreases, until a steady state is reached. Then the disc rotates at a constant speed, and the frictional torque is balanced by the torque Π produced. The effect of viscosity on the harvester performance is investigated by replacing the air flow with rainwater, as discussed later.

To gain insight on the aerodynamic torque generated by injecting the air to drive the discs to rotate, numerical simulations are conducted by using ANSYS CFX [28,30]. The working fluid is assumed to be ideal gas. And it satisfies the equation of state:

$$\frac{p}{\rho} = RT = \frac{c^2}{\gamma} \quad (3)$$

Fig. 3 illustrates the CFX-mesh used to iteratively solve the system equations [28,30]. The CFX solver setting used in our simulations is described in the table in Appendix. It is worth noting that a finer structured mesh is generated at the vicinity of the disc wall (boundary layer) for accurate solution. There are 11 nodes used in the axial direction between two neighboring discs to capture the boundary layer superposition. The disc edges with the desired intervals and ratio of increasing or decreasing the cell width are meshed first. The thickness of the boundary layer for turbulent flow at zero angle of incidence [28] is approximated by using $\delta_b = 0.036 \mathcal{L} (\mu / \rho U \mathcal{L})^{1/5}$. Here \mathcal{L} is the length downstream from the start of the disc, and U is the fluid's bulk velocity. In the axial direction $-\delta_b < z < \delta_b$, the region near the disc wall is not movable.

The flow is assumed to be three dimensional and turbulent. The state-of-the-art CFD code employs a control volume based finite

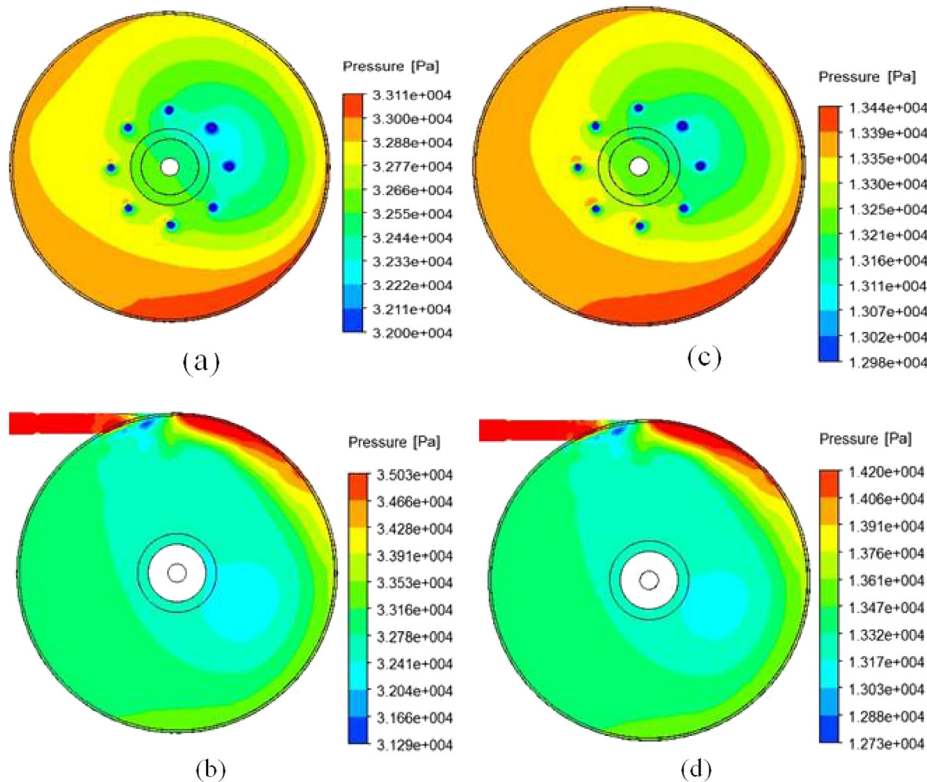


Fig. 4. Calculated pressure distribution along the side- (a) and (c) and centering-disc (b) and (d): (a)–(b) the volume flow rate is set to 0.00502 m³/s, (c)–(d) the volume flow rate is set to 0.00328 m³/s.

element method to solve the unsteady conservation equations as given as:

(1) mass conservation:

$$\frac{\partial \rho}{\partial t} + \nabla \cdot (\rho \mathbf{U}) = 0 \quad (4)$$

(2) Momentum conservation:

$$\frac{\partial \rho \mathbf{U}}{\partial t} + \nabla \cdot (\rho \mathbf{U} \times \mathbf{U}) = -\nabla p + \nabla \cdot \tau \quad (5)$$

(3) Energy conservation:

$$\frac{\partial \rho H_{\text{tot}}}{\partial t} - \frac{\partial p}{\partial t} + \nabla \cdot (\rho \mathbf{U} H_{\text{tot}}) = \nabla \cdot (\lambda \nabla T) + \nabla \cdot (\mathbf{U} \cdot \tau) \quad (6)$$

where H_{tot} is the total enthalpy. It is related to the static enthalpy $H(T, \rho)$ by $H_{\text{tot}} = H + \mathbf{U}^2/2$. T is temperature, λ denotes the thermal conductivity and τ is the stress tensor and it is related to the strain rate by

$$\tau = \mu \left(\nabla \mathbf{U} + (\nabla \mathbf{U})^T - \frac{2}{3} \delta \nabla \cdot \mathbf{U} \right) \quad (7)$$

where δ is the identity matrix. Superscript T denotes the transpose.

As the coupled system equations are solved, the pressure distribution along the surface of discs placed at two different locations are predicted, as shown in Fig. 4. It can be seen that as the inlet volume flow rate is set to two different values, the pressure distributions are similar (see Fig. 4(a) and (c) or Fig. 4(b) and (d)). However, the maximum pressure is different. And the different pressure distributions of the disc surfaces reveal that the pressure gradient is present. In addition, as the air moves towards the center of the disc, its radial pressure decreases due to the gradual decrease of the flow area and increased radial velocity. The pressure gradient ensures the shear stress being generated and so the aerodynamic torque to drive the discs to rotate. The present simulations by using ANSYS CFX shed light on the physics and working principles of the disc-involved harvester. However, no comparison is made between the numerical and experimental results, since the measurements are conducted in terms of the electrical output power only.

As the torque Π generated drives the compact discs to rotate, the shaft and the magnet attached at its end rotate too. The rotation of the magnet in a wound coil of copper gives rise to the electrical power being generated due to the magnetic flux change in the coil [31]. If emf (electromotive force) measured is varied sinusoidally

with time, then the current and the output power of the closed-loop electrical circuit is an alternating one as given as

$$I = \frac{\mathcal{U}_N}{R_{\text{tot}}}, \quad \text{and} \quad E = \frac{\mathcal{U}_N^2}{R_{\text{tot}}} \quad (8)$$

where R_{tot} is the total resistance of the closed-loop electrical circuit. The emf generated \mathcal{U}_N is due to the magnetic flux changed in the copper wire loop, which is stationary in our experiment and has N turns. And \mathcal{U}_N is equal to the rate of change of the magnetic flux through the circuit surface \mathbf{S} . Following the Maxwell–Faraday's law [31] $-\nabla \times \mathbf{E} = \partial \mathbf{B} / \partial t$ and by using Stokes' theorem, \mathcal{U}_N can be determined in integral form as

$$\mathcal{U}_N = N \oint_{\mathcal{T}} \mathbf{E} \cdot d\mathbf{s} = N \int_{\mathbf{S}} (\nabla \times \mathbf{E}) \cdot \mathbf{n} dA = -N \frac{\partial}{\partial t} \int_{\mathbf{S}} \mathbf{B} \cdot \mathbf{n} dA \quad (9)$$

where \mathcal{T} is a closed curve, \mathbf{S} is the surface bounded by it, \mathbf{E} is the electric field and \mathbf{B} is the magnetic field. Here we assume that emf generated from each turn of the coil is equal. Substituting Eq. (9) into Eq. (8) leads to

$$E = N^2 \frac{\left[\frac{\partial}{\partial t} \left(\int_{\mathbf{S}} \mathbf{B} \cdot \mathbf{n} dA \right) \right]_{\text{max}}^2}{2R_0} = N \frac{\left[\frac{\partial}{\partial t} \left(\int_{\mathbf{S}} \mathbf{B} \cdot \mathbf{n} dA \right) \right]_{\text{max}}^2}{2R_i} \quad (10)$$

It can be seen that and the power generated is N^2 times larger than the wound coil of copper with 1 turn, as $R_0 = NR_i$ remains constant. Eq. (10) suggests that the power output E can be increased by increasing the copper wire turn number N . In addition, when N remains unchanged, the output voltage \mathcal{U}_N and power E are related to the rate of change of the magnetic flux as,

$$\mathcal{U}_N \propto \frac{\partial(\cdot)}{\partial t}, \quad \text{and} \quad E \propto \left(\frac{\partial(\cdot)}{\partial t} \right)^2 \quad (11)$$

These relationships are validated from our experimental measurements as shown in the following sections.

2.3. Measurement configurations and design parameters

Generally, there are two configurations to measure the electrical power output from the harvester. One is open-loop electrical circuit, as shown in Fig. 5(a). A multimeter is directly applied to measure the voltage output and power. The coil wire resistance is denoted by R_0 . The other configuration is to connect a known resistor with resistance R_L to build a closed-loop electrical circuit. By measuring the voltage across the resistor, the electrical current and power output from the energy harvester are estimated. The two-configuration measurements are performed in case some of the researchers/readers might be interested in the electric current, which can be measured in closed-loop configuration.

There are 4 design parameters as described in Table 1, which play critical roles in determining the harvester performance. The effect of each given parameter is studied later by conducting a parametric measurement of the electrical power output.

3. Experimental results

3.1. Open-loop parametric measurements

The power output E_0 as shown in Eq. (10) will be increased by increasing the copper wire number of turns N . This is confirmed

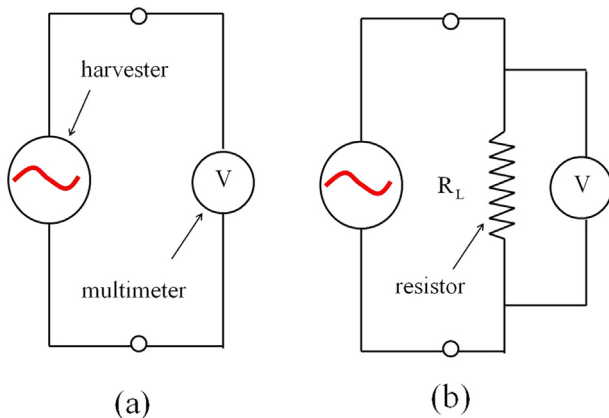


Fig. 5. Open- and closed-loop electrical circuits built by the energy harvester and the loading resistor.

Table 1
Design parameters to be studied.

| Parameters | Names | Unit |
|---------------|------------------------|------|
| \mathcal{D} | Disc diameter | mm |
| Δd | Inter-disc distance | mm |
| \mathcal{N} | The number of discs | |
| \mathcal{J} | The number of orifices | |

from our experimental measurements, as shown in Fig. 6. It illustrates the variation of the output RMS (root mean square) voltage and power with the inlet volume flow rate set to 4 different values, as N is set to 280 and 560 respectively. It can be seen that the output power and voltage from the 560 turns coil is approximately twice that of 280 turns. This is most likely because the resistance is proportional to the length of the copper coil i.e. $R_0/N \approx R_i$. And so $E_0 \propto N$. It is worth noting that the discharge of the air flow is determined by measuring the cross-sectional area of the inlet nozzle and the average velocity of the air flow. For this, a constant temperature HWA (hot wire anemometry) is placed near a sidewall exhaust orifice. By assuming that the volume flow rate from the exhaust orifice is the same as others, and that there is no air leakage from the turbine, the air flow velocity can be predicted. Before implemented, the hot wire probe is calibrated in a wind tunnel at the Fluid Mechanics Laboratory in Nanyang Technological University. The probe is connected to a mini CTA 54T30 system from DANTEC dynamics which is linked up with a data acquisition card from National Instruments NI USB6008.

As indicated in Eq. (11), the output voltage and power are shown to be related to the rate of change of the magnetic flux. Fig. 7 shows the variation of the electrical output from the 80 mm harvester with RPM (revolutions per minute). Note that the electrical power output E_0 as measured by using Fluke digital multimeter is calculated by the following equation $E_0 = V_{\text{rms}}^2/R_0 = V_0^2/2R_0$, where $V_{\text{rms}} = V_0/\sqrt{2}$ denotes the RMS (root mean square) of the output voltage V_0 . It can be seen that the output RMS voltage and power E_0 are increased linearly and quadratically with increased RPM, as measured by using AI3030 Tachometer. The maximum power output can reach to approximately 0.3 Watt at $\text{RPM} \approx 6300$.

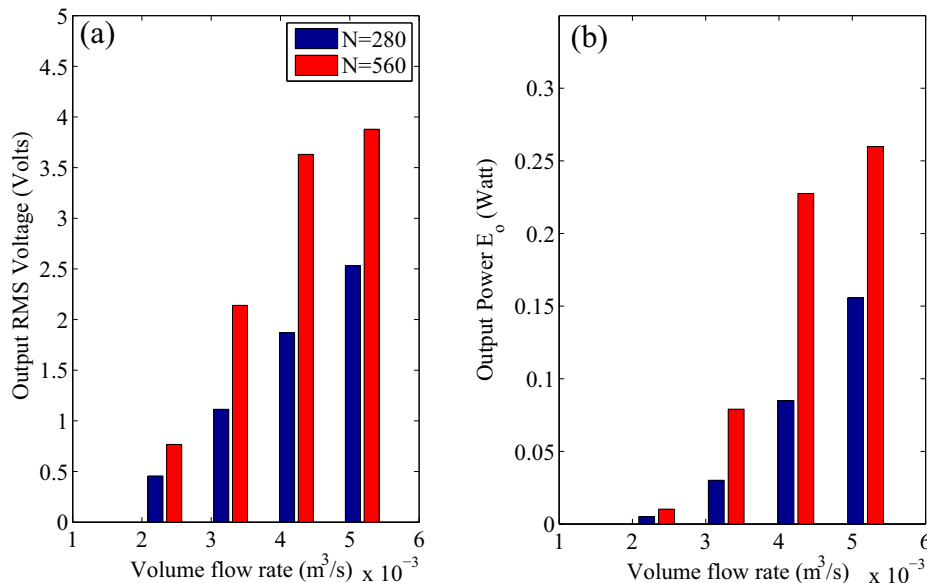


Fig. 6. Comparison of the measured voltage and power output from the 80 mm air-driven harvester, as N is set to 280 and 560 respectively.

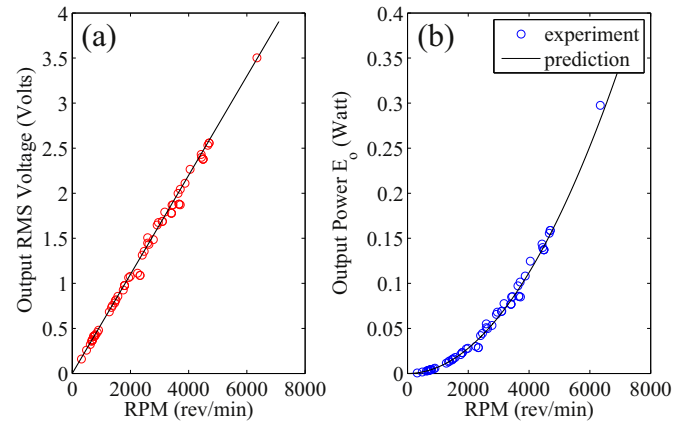


Fig. 7. Variation of output RMS voltage and power from the 80 mm harvester with revolutions per minute (RPM) of the discs.

Fig. 8(a) illustrates time evolution of the instantaneous measurement of the AC voltage, as measured by using Tektronix TDS1012B digital oscilloscope (100 MHz). There are 2 different regions in the oscilloscope trace of the acquired signal: the transient stage due to the inertia effect $t < 30$ s and the stable stage $t > 30$ s, where 'saturated' emf is produced and used to calculate the power output.

In order to highlight the effects of the system parameters on its performance and to gain insight on its optimum design, a parametric measurement is then conducted. The parameters involve the disc diameter \mathcal{D} , the number of discs \mathcal{N} , the distance between two neighboring discs Δd , and the number of orifices \mathcal{J} characterizing the exhaust flow rate, as shown in Table 1. Fig. 9 illustrates the variation of the output electrical power with the system parameters. It can be seen that the output power is increased with the increased inlet volume rate. When the discs' diameter or number is increased, the output power is increased, as shown in Fig. 9(a) and (b) respectively. However, there are optimum values of inter-disc distance and the sidewall orifices' number, which correspond to the maximum power output. When the inlet volume flow rate is smaller, the optimum Δd and \mathcal{J} are around 0.5 mm and 8

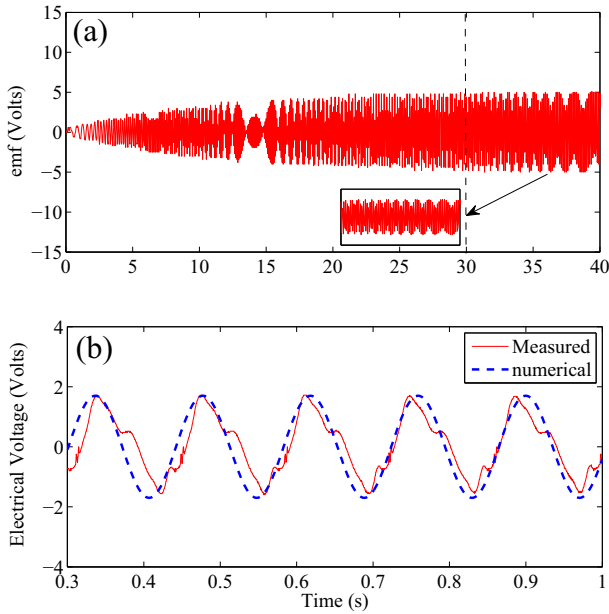


Fig. 8. Measured emf from the 80 mm energy harvester driven by air flow.

respectively, as shown in Fig. 9(c) and (d). The optimum values are used later in the design of rainwater-driven harvester.

3.2. Closed-loop measurements

The electrical power output can also be measured by connecting a resistor, as shown in Fig. 5(b). Theoretically, when the resistor's

resistance is equal to that of the copper wires, maximum power output is obtained. The variations of measured output RMS voltage and power are shown in Fig. 10. It can be seen that the RMS voltage output is increased with increased loading resistance R_L . However, the output power reaches a maximum value when $R_L = 146$ Ohms. This loading resistance is closed to the resistance of the copper wire. In addition, the corresponding maximum current is approximately 40 mA.

4. Rainwater-driven harvester

The potential application of such bladeless system for energy harvesting is investigated by using rainwater, collected and stored in a water tank with a volume of 20 L, as shown schematically in Fig. 11(a). A soft PVC pipe with a diameter D of 6.25 mm is used to connect the water tank and a bladeless harvester, as shown in Fig. 11(b). Three different-diameter harvesters are tested. And the minimum diameter of the disc is 40 mm, as shown in Fig. 11(c).

By placing the water tank at about 2 m away from the ground, a flow with approximately 3.6 m/s is generated. The water flow average velocity is measured by using volumetric method via knowing the cross-sectional area of the inlet nozzle with a diameter 6.0 mm and determining the time (about 9.7 s) taken to discharge 1000 ml water. The measured flow velocity can also be theoretically approximated by using Bernoulli equation [32] as

$$\frac{\Delta p}{\rho_w g} + \Delta \mathcal{H} = \frac{\Delta v^2}{2g} + \sum \epsilon_i \frac{\Delta v^2}{2g} \quad (12)$$

where ρ_w is the water density, g is the gravitational acceleration, $\Delta p \approx 0$ due to the fact that the water discharges into the atmosphere and the water in the tank is open to the atmosphere. $\Delta \mathcal{H} = 1.96$ m is the elevation difference between the water level in the

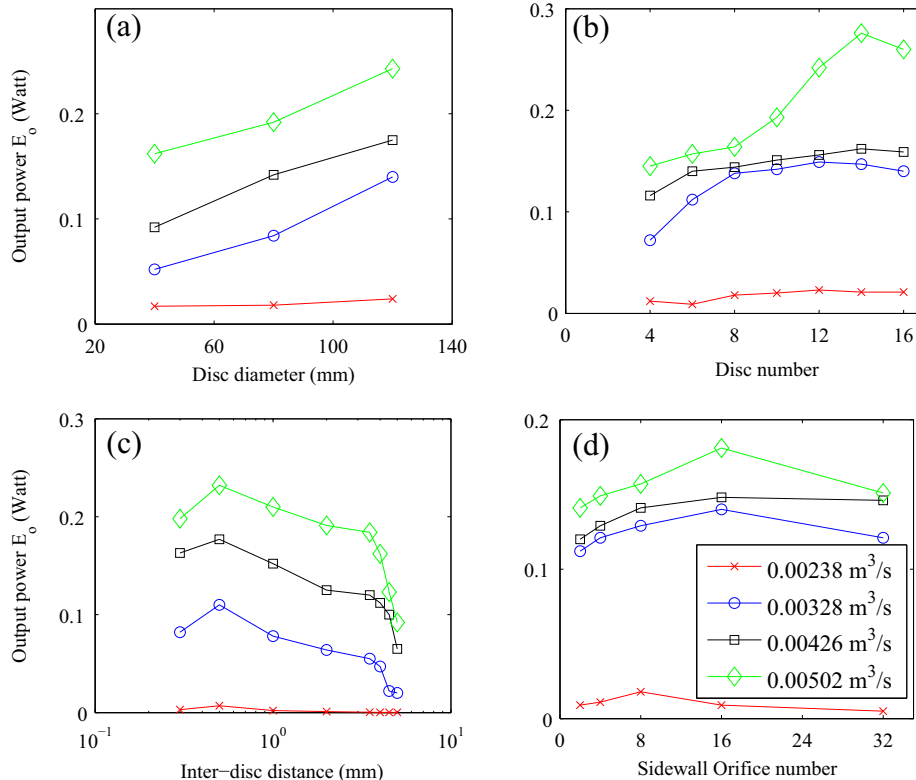


Fig. 9. Variation of the output electrical power with the system parameters (a) disc diameter D , (b) the number of discs N , (c) inter-disc distance Δd and (d) the number of exhaust orifices \mathcal{J} , as the inlet volume flow rate is set to four-different values.

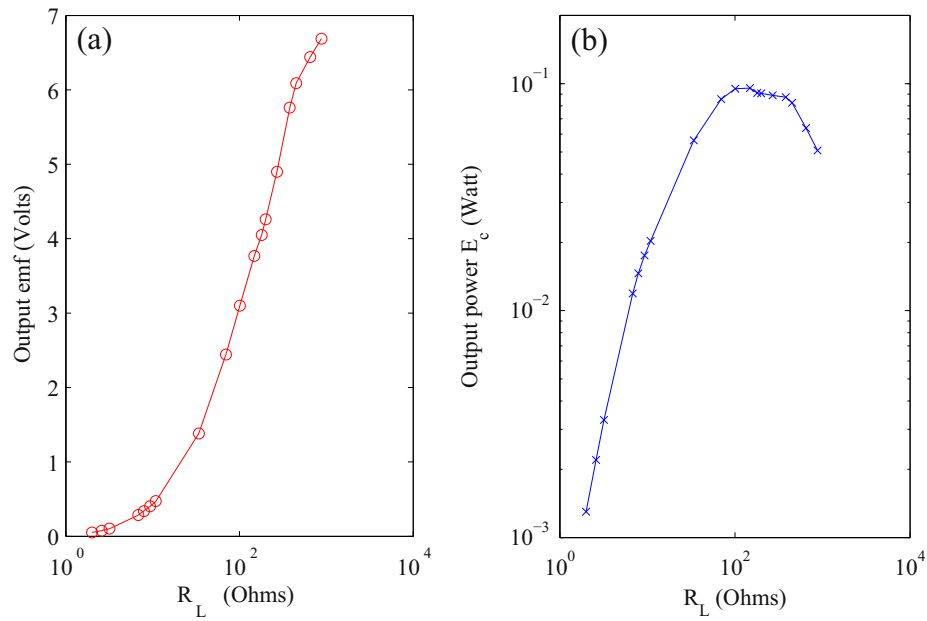


Fig. 10. Measured electrical circuit voltage and power from the 80 mm air-driven harvester with varying resistance R_L , as $N = 280$.

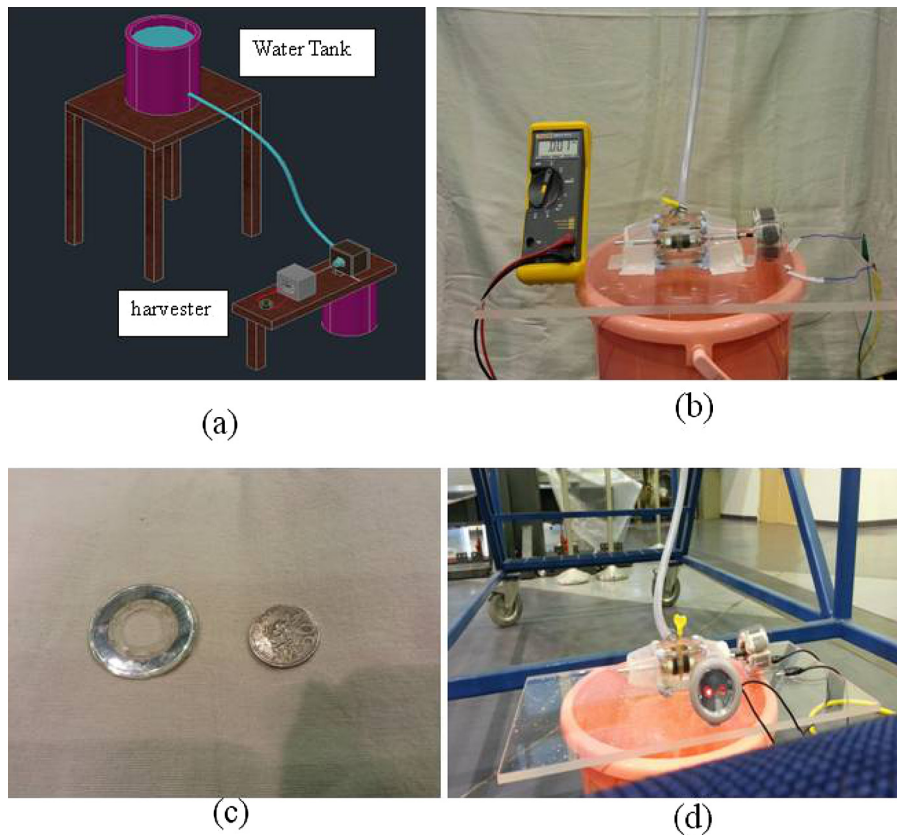


Fig. 11. (a) schematic of the experimental setup, (b) experimental setup of the 40 mm rainwater-driven harvester, (c) Comparison of a 40 mm rotating disc with a 50 cent Singapore coin and (d) a red LED is powered by the 40 mm harvester (please refer to the video attached).

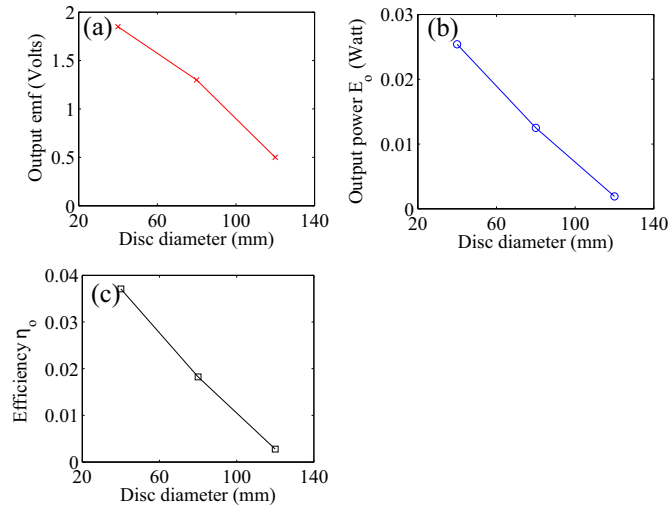


Fig. 12. Measured open-loop output voltage, power and efficiency η_o , as the disc diameter in the rainwater-driven harvester is set to 40, 80 and 120 mm respectively.

water tank and the turbine inlet, Δv^2 is the kinetic energy difference between the free surface of the water tank and outlet of the pipe. However, since the tank is large relative to the pipe outlet, the 'free surface' velocity is zero (assumed stationary in the tank), Δv is the outlet velocity. $\sum \varepsilon_i$ is the total head loss coefficient. And it consists of the entrance loss ε_1 , entrance elbow loss ε_2 and friction loss ε_3 . Here $\varepsilon_1 = 0.8$ and $\varepsilon_2 = 0.3$ are empirically selected [32]. The friction loss $\varepsilon_3 = f(L/D)$, as indicated in Darcy–Weisbach energy loss equation depends on the pipe length L and diameter, D . f is the pipe friction factor. It depends on the Reynolds number and the pipe surface roughness ξ as

$$f = \mathcal{F}\left(\text{Re}, \frac{\xi}{D}\right) \quad (13)$$

Here $f = 7.54 \times 10^{-3}$ is the friction factor determined from the Moody diagram. By using these values, the estimated flow velocity is about 3.4 m/s. The corresponding Reynolds number is

$$\text{Re} = \frac{\rho_w \Delta v D}{\mu_w} = 1.9 \times 10^4 \quad (14)$$

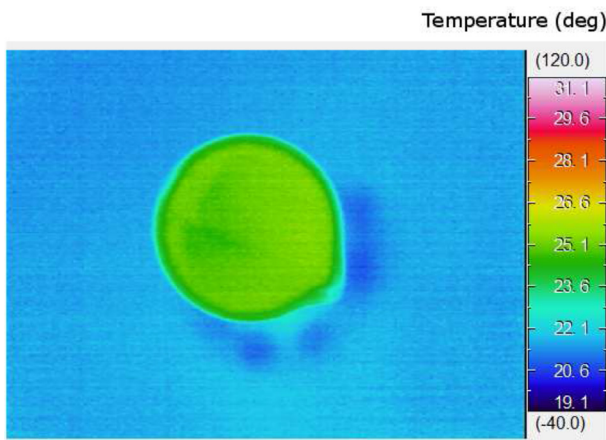


Fig. 13. Measured rainwater temperature contour by using an infrared thermal imaging camera.

The inlet flow is turbulent. As the water is injected in the bladeless system, electrical power is produced. The electric power harnessed from the rainwater with density 991.65 kg/m^3 at 23.8°C as shown in Fig. 13 can be used for many purposes. For convenience, however, the energy harvester is coupled with a red LED (light-emitting diode) for demonstration, as shown in Fig. 11(d). The application indicates that the miniature harvester provides a simple, low-cost but robust platform to harvest the mechanical energy of rainfall to generate electricity, as shown in Fig. 8(b).

To characterize the harvester performance, the overall energy conversion efficiency η_o in open-loop configuration is defined as

$$\eta_o = \frac{E_o}{E_i} = \frac{V_o^2 / 2R_o}{\dot{m}_w \Delta v^2 / 2} \quad (15)$$

It describes the fraction of total input kinetic energy being converted into electrical power. Fig. 12(c) shows the variation of η_o with the disc diameter D . It can be seen that η_o is decreased with increased disc diameter D . Similar trends are observed in the measured output voltage and power, as shown in Fig. 12(a) and (b) respectively. Such overall efficiency (also known as Brayton cycle thermal efficiency) is used to characterize a conventional miniature gas turbine [28]. And it is shown that η_o is approximately 2%–3%, which is slightly lower than the performance of the present 40 mm harvester.

When a known resistor is connected to the harvester, a closed-loop electrical circuit is built. The electrical power produced can be calculated by measuring the voltage and current through the resistor. Fig. 14(a) and (b) show the closed-loop measurements of the output voltage and power from the 40 mm rainwater-driven harvester. It can be seen that the output voltage U_c is increased with the loading resistance R_L . However, maximum power output E_c occurs, when the loading resistance is closed to the internal resistance of the harvester, i.e. $R_L \approx 146 \text{ Ohms}$. Furthermore, U_c and E_c from the energy harvesting system with 8 discs i.e. $\mathcal{N} = 8$ is much larger than that from the 4 disc system. Same trend is observed in the measured overall efficiency $\eta_c = E_c/E_i$, as shown in Fig. 14(c). Finally, the performance of the 40 mm harvester driven by rainwater is compared with that driven by air flow in terms of the efficiency η_c , as shown in Fig. 14(d). It is apparent that the efficiency η_c of the rainwater-driven harvester is much higher than that of the same size air-driven one. This could be due to the increased viscosity, i.e. $\mu_w > \mu_a$. As indicated in Eqs. (1) and (2), the torque will be increased with increased shear stress (viscous drag). This reveals the critical role of the viscosity being played in determining the performance of the miniature harvester.

It is worth noting that these small-scale harvesters are driven by water, which could be from rainfall or river. However, they are designed to maximize the abstraction of rainwater collection from airport or residential buildings in Singapore with abundant rainfall.

5. Discussion and conclusions

In summary, we demonstrate the feasibility of harvesting the kinetic energy of turbulent air and rainwater flow by using three different diameter bladeless systems. They provide a simple platform to produce electrical power via using a number of co-rotating discs. These harvesters work basing on the flow physics that a shear stress force and torque are generated due to the velocity gradient present between a compact disc and working fluid. To study the aerodynamics of the rotating discs driven by injecting turbulent air flow, numerical simulations are conducted. Our present systems are bladeless electromagnetic-coupling ones. And they can be used for both air and water flows. This is

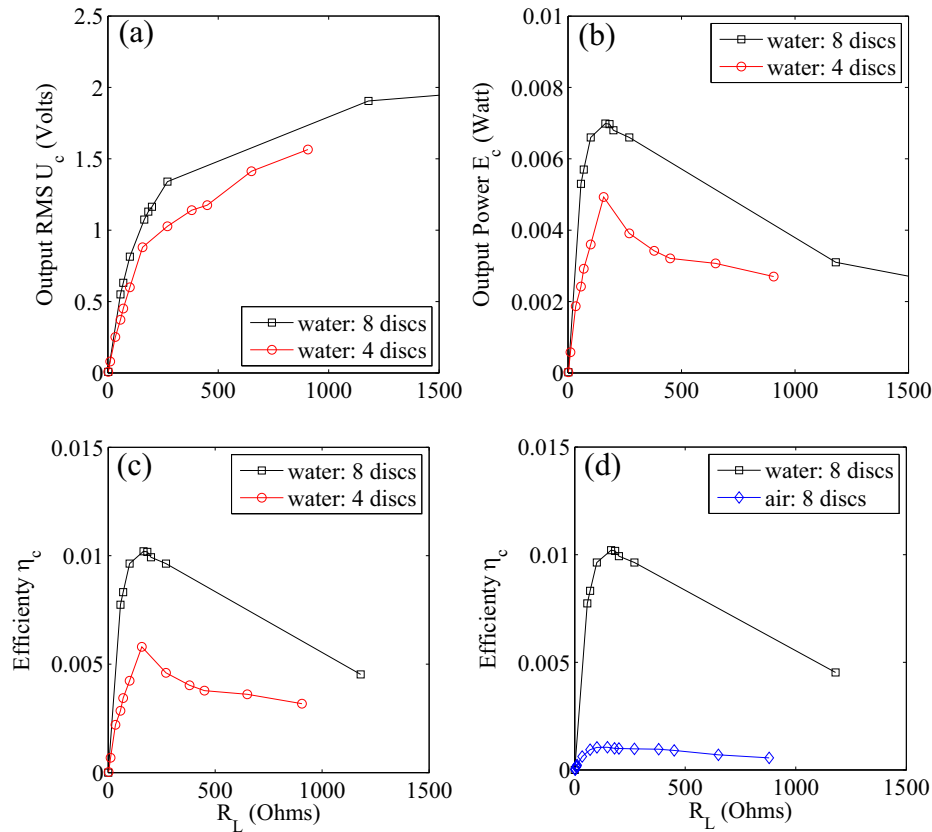


Fig. 14. Measured electrical circuit voltage and power from the 40 mm rainwater-driven harvester with varying resistance R_L , as $R_0 = 146$ Ohm.

different from the conventional blade-involved systems. The experimental results obtained by measuring the system responses for 4 different levels of air flow excitations show that about 0.3 Watt electrical power is generated. Parametric measurement of the harvester performance is then conducted in terms of the disc number, diameter, the exhaust flow rate and the inter-disc distance. Finally, a 40 mm bladeless system is experimentally tested to harvest energy from rainwater. It is found that the rainwater-driven harvester works more efficiently than the same-size air-driven one. This is most likely due to the dramatically increased viscosity. Moreover, the overall energy conversion efficiency is found to be approximately 2%–3%. It is slightly higher than a conventional miniature gas turbine. The overall efficiency is also shown to decrease with increased disc diameter D . The maximum electric current from the 40 mm water-driven harvester is 4.5 mA. In order to demonstrate its practical application, the electricity generated is used to power a red LED. The present study reveals the potential of implementing such small-scale systems for rainwater energy harvesting in tropical countries with abundant rainfall, like Singapore.

Acknowledgements

This work is supported by Singapore Ministry of Education, AcR-Tier1-RG91/13-M4011228.050. This financial support is gratefully acknowledged. We would like to thank Mr. J. Khoo for his precious contribution in building the rig and carrying out the experimental measurements. We wish to thank the anonymous reviewers for their useful comments.

Appendix A

Table 1

CFX solver setting used in ANSYS.

| Mesh type | Hexahedral |
|---------------------------|-----------------|
| Fluid | Air |
| Turbulence model | $k-\epsilon$ |
| Inlet boundary condition | Velocity inlet |
| Outlet boundary condition | Pressure outlet |
| Number of element | 1,841,356 |
| Number of node | 320,303 |

Table 2

Measured density ratio of rainwater ρ_w with respect to tap water ρ_t by using volumetric method.

| Measured volume (ml) | | Net weight (gram) | | Density ratio ρ_w/ρ_t |
|----------------------|-----------|-------------------|-----------|----------------------------------|
| Rainwater | Tap water | Rainwater | Tap water | |
| 400 | 400 | 392.47 | 391.26 | 1.0031 |
| 700 | 700 | 696.70 | 692.96 | 1.0068 |
| 1000 | 1000 | 997.07 | 995.97 | 1.0012 |

Nomenclature

| | |
|-----|--|
| A | cross-sectional area of wound coil wire, m^2 |
| B | magnetic field, T |

| | |
|------------------|--|
| c | speed of sound, m/s |
| \mathcal{D} | disc diameter, mm |
| D | pipe diameter, mm |
| Δd | inter-disc distance, mm |
| ΔH | height elevation, m |
| E_o | output electrical power, Watt |
| η_o, η_c | open- and closed-loop overall energy conversion efficiencies |
| E | electric field, V/m |
| E_i | input total kinetic power, Watt |
| H | static enthalpy, J |
| I | electrical current, Amp |
| \mathcal{J} | number of exhaust orifices |
| \dot{m}_w | water flow rate, Kg/s |
| N | number of coil turns |
| p | pressure, Pa |
| Π | aerodynamic torque, N·m |
| \dot{Q} | water volume flow rate, m^3/s |
| R | Gas constant, J/mol·K |
| R_o, R_L | harvester internal and loading resistance, Ohms |
| ρ_a, ρ_w | air and water density, kg/m^3 |
| Re | Reynolds number |
| τ_w | shear stress, Pa |
| τ | the viscous stress tensor, N/m |
| λ | conduction coefficient, W/m K |
| T | temperature, K |
| \mathcal{U}_N | output voltage, V |
| U | air flow velocity, m/s |
| μ | viscosity coefficient, Pa·s |

Subscript

| | |
|-------|------------------|
| o | open-loop |
| c | closed-loop |
| tot | total resistance |

References

- [1] Zhao D. Waste thermal energy harvesting from a convection-driven Rijke-Zhao thermo-acoustic-piezo system. *Energy Convers Manag* 2012;66(1): 87–97.
- [2] Zhao D. Transient growth of flow disturbances in triggering a Rijke tube combustion instability. *Combust Flame* 2012;159:2126–37.
- [3] Li SH, Zhao D. Heat flux and acoustic power in a convection-driven T-shaped thermoacoustic system. *Energy Convers Manag* 2013;75:336–47.
- [4] Moldenhauer S, Stark T, Holtmann C, Thess A. The pulse tube engine: a numerical and experimental approach on its design, performance, and operating conditions. *Energy* 2013;55:703–15.
- [5] Zhao D, Ji C, Li S, Li J. Thermodynamic measurement and analysis of dual-temperature thermoacoustic oscillations for energy harvesting application. *Energy* 2014;65:517–26.
- [6] Bisio G, Rubatto G. Sondhaus and Rijke oscillations—thermodynamic analysis possible applications and analogies. *Energy* 1999;24(2):117–31.
- [7] Chun W, Oh SJ, Lee YJ, Lim SH, Surathu R, Chen K. Acoustic waves generated by a TA(thermoacoustic) laser pair. *Energy* 2012;45(1):541–5.
- [8] Markides CN, Smith TC. A dynamic model for the efficiency optimization of an oscillatory low grade heat engine. *Energy* 2011;36(12):6967–80.
- [9] Zhao D, Chew Y. Energy harvesting from a convection-driven Rijke-Zhao thermoacoustic engine. *J Appl Phys* 2013;112:87–97.
- [10] Grasland-Mongrain P, Mari J, Gilles B, Chapelon J. Electromagnetic hydrophone with tomographic system for absolute velocity field mapping. *Appl Phys Lett* 2012;100:234502.
- [11] Vocca H, Neri I, Travasso F, Gammaitoni L. Kinetic energy harvesting with bistable oscillators. *Appl Energy* 2012;97:771–6.
- [12] Liu H, Zhang S, Kathiresan R, Kobayashi T. Development of piezoelectric microcantilever flow sensor with wind-driven energy harvesting capability. *Appl Phys Lett* 2012;100:223905.
- [13] Xiao J, Yang T, Li P, Zhai P, Zhang Q. Thermal design and management for performance optimization of solar thermoelectric generator. *Appl Energy* 2012;93:33–8.
- [14] Gou X, Xiao H, Yang S. Modeling experimental study and optimization on low-temperature waste heat thermoelectric generator system. *Appl Energy* 2010;87:3131–6.
- [15] Firtin E, Guler O, Akdag SA. Investigation of wind shear coefficients and their effect on electrical energy generation. *Appl Energy* 2011;88:4097–105.
- [16] Arifujaman M, Iqbal M, Quaique JE. Energy capture by a small wind-energy conversion system. *Appl Energy* 2008;85:41–51.
- [17] Sayed MA, Kandil HA, Shaltot A. Aerodynamic analysis of different wind-turbine-blade profiles using finite-volume method. *Energy Convers Manag* 2012;64:541–50.
- [18] Ozgener D. A small wind turbine system (SWTS) application and its performance analysis. *Energy Convers Manag* 2006;47:1326–37.
- [19] Bishop JDK, Amaratunga GAJ. Evaluation of small wind turbines in distributed arrangement as sustainable wind energy option for Barbados. *Energy Convers Manag* 2008;49:1652–61.
- [20] Perkovic L, Silva P, Ban M, Kranjcevic N, Duic N. Harvesting high altitude wind energy for power production: the concept based on Magnus effect. *Appl Energy* 2013;101:151–60.
- [21] Sengupta S, Guha A. A theory of Tesla disc turbines. *Proc IMechE Part A J Power Energy* 2012;226:650–63.
- [22] Guha A, Sengupta S. The fluid dynamics of the rotating flow in a Tesla disc turbine. *Euro J Mech-B/Fluids* 2013;37:112–23.
- [23] Hoya GP, Guha A. The design of a test rig and study of the performance and efficiency of a Tesla disc turbine. *Proc IMechE Part A J Power Energy* 2009;223:451–65.
- [24] Lampart P, Jedrzejewski L. Investigations of aerodynamics of Tesla bladeless microturbines. *J Theo Appl Mech* 2011;49:477–99.
- [25] Choon TW, AnasRahman A, Li TS, Aik LE. Tesla turbine for energy conversion. *IEEE Malaysia Power Energy*; 2012:820–5.
- [26] Carey VP. Computational/theoretical modeling of flow physics and transport in disk rotor drag turbine expanders for green energy conversion technologies. *Proc ASME Inter Mech Eng Cong Expo* 2012;11:31–8.
- [27] Tesla N. Tesla turbine, US Patent 1061206, May 6 1913.
- [28] Deam RT, Lemma E, Mace B, Collins R. On scaling down turbines to millimeter size. *J Eng Gas Turb Power* 2008;130:052301.
- [29] Zhao D, Khoo J. Rainwater- and air-driven 40mm bladeless electromagnetic energy harvester. *Appl Phys Lett* 2013;103:033904.
- [30] ANSYS. CFX-Solver Theory Guide (Release 12.0). Canonsburg: ANSYS Inc.; 2009.
- [31] Feynman RP, Leighton RB, Sands M. The Feynman lectures on physics. Boston, USA: Addison Wesley Longman; 1970.
- [32] White FM. Fluid Mechanics. 7th ed. Singapore: McGraw-Hill International; 2003.